NRC Publications Archive
Archives des publications du CNRC

Polarization analysis for metal-supported SOFCs from different fabrication processes

Huang, Qiu-An; Oberste-Berghaus, Jörg; Yang, Dongfang; Yick, Sing; Wang, Zhenwei; Wang, Bingwen; Hui, Rob

NRC Publications Record / Notice d'Archives des publications de CNRC:
https://nrc-publications.canada.ca/eng/view/object/?id=2f9da77d-9000-4952-8a4e-98ef2025f433
https://publications-cnrc.canada.ca/fra/voir/objet/?id=2f9da77d-9000-4952-8a4e-98ef2025f433

Questions? Contact the NRC Publications Archive team at
PublicationsArchive-ArchivesPublications@nrc-cnrc.gc.ca. If you wish to email the authors directly, please see the first page of the publication for their contact information.

Vous avez des questions? Nous pouvons vous aider. Pour communiquer directement avec un auteur, consultez la première page de la revue dans laquelle son article a été publié afin de trouver ses coordonnées. Si vous n'arrivez pas à les repérer, communiquez avec nous à PublicationsArchive-ArchivesPublications@nrc-cnrc.gc.ca.

National Research Council Canada   Conseil national de recherches Canada

Polarization Analysis for Metal-Supported SOFCs from Different Fabrication Processes

Qiu-An Huang[a, b, z], Jörg Oberste-Berghaus[c], Dongfang Yang[d], Sing Yick[a], Zhenwei Wang[a],

Bingwen Wang[b], Rob Hui[a, *]

[a] *Institute for Fuel Cell Innovation, National Research Council Canada, 4250 Wesbrook Mall, Vancouver, B.C. V6T 1W5 Canada*

[b] *Department of Control Science and Engineering, Huazhong University of Science and Technology, Wuhan, Hubei, 430074, P.R. China*

[c] *Industrial Materials Institute, National Research Council Canada, 75 de Mortagne, Boucherville, Québec, J4B 6Y4 Canada*

[d] *Industrial Materials Institute, National Research Council Canada, 800 Collip Circle, London, O.N. N6G 4X8 Canada*

* *Corresponding author. Tel.: +1 604 221 3111; Fax: +1 604 221 3001.*

E-mail address: Rob.Hui@nrc-cnrc.gc.ca (R. Hui)

[z] *Permanent address: Faculty of Physics and Electronic Technology, Hubei University, Wuhan, Hubei, 430062, P.R. China*

Abstract

Polarization characteristics of metal-supported solid oxide fuel cells, fabricated by both pulsed laser deposition and suspension plasma spray, were investigated. With the electrochemical impedance spectroscopy and current-voltage polarization curves, the metal-supported SOFCs were compared and analyzed in term of their cathode exchange current density, polarization loss and maximum power density over the temperature range of $400\sim600^{\circ}C$. The electrochemical mechanism for the linear polarization characteristics observed from the experimental data was addressed. Results from the experiment and simulation studies indicate that fabrication processes and operation temperatures play a key role in the electrochemical mechanism for linear polarization characteristics of metal-supported SOFCs.

1. Introduction

Solid oxide fuel cells (SOFCs) are expected to be highly favourable for stationary power generation due to their high efficiency, low/zero pollution and fuel flexibility. However, high cost and low durability/reliability are major barriers in the path towards SOFC commercialization. It has been recognized that both these barriers are primarily due to the high temperature operation [1].

In an effort to overcome these barriers, recently, SOFCs with reduced operation temperature (500~850°C) have received increasing interest. SOFCs operating at lower temperatures exhibit numerous advantages such as wider choice of low-cost component materials, improved stability, and increased flexibility in the structure design [2]. As a representative of SOFC family, metal-supported SOFCs are expected to be more competitive than traditional energy conversion technologies due to the low cost, high strength, better workability, good thermal conductivity, and quicker start-up [3]. However, their performance is still relatively low at this current technology stage.

With respect to the development of reduced temperature SOFC technology, reducing electrolyte thickness and developing alternative materials with high ion conductivity at reduced temperature are two major approaches. So far, various processing technique, including spray pyrolysis (SP) [4], [5], pulse laser deposition (PLD) [6]-[8], and suspension plasma spray (SPS) [9], [10], as well as spray and spin coating [11]-[13], have been extensively explored. These

processing techniques have significant effect on the SOFC interfacial morphology, determining the SOFC performance.

For performance improvement and component optimization of SOFCs, fundamental understanding of the correlation between fabrication processes and fuel cell reaction kinetics including analysis of polarization characteristics seems to be necessary [14]-[19]. However, for metal-supported SOFCs, there is very little literature focusing on fundamental understanding, in particular, through polarization analysis assisted by electrochemical impedance spectroscopy (EIS) [20].

In our previous work [8], EIS and electrochemical polarization were employed to investigate the performance and aging characteristics for metal-supported SOFCs, named Cell #1, with samarium doped ceria (SDC)/scandia-stabilized zirconia (ScSZ) bilayer as electrolytes, fabricated by PLD. However, in-depth analysis of the polarization characteristics was not pursued in the paper. In the continuing effort to optimize the fabrication process and to improve the SOFC performance, a comprehensive analysis based on EIS data and polarization curves is given in this paper at temperatures of 400~600°C. Two representative metal-supported SOFC single cells, previous Cell #1 [8] and recently Cell #2 fabricated by suspension plasma spray, were chosen as examples for such a purpose.

2. Experimental Procedures

Metal-supported SOFC single cells were fabricated using different deposition techniques. Commercially available porous SS430 and porous Hastelloy X alloys were adopted as substrates

for selected Cell #1 and Cell #2, respectively. Porosity measurements of the SS430 and Hasteloy X were performed using the Archimedes method and their values were 22% and 28% respectively. Cell #1 consists of NiO-SDC (50% in wt.%) as the anode, ScSz and SDC bi-layer as the electrolyte, and $Sm_{0.5}Sr_{0.5}CoO_{3-\delta}$ (SSCo)-SDC (weight ratio 75:25) as the cathode. Cell #2 consists of NiO-SDC (50% in wt.%) as the anode, SDC as the electrolyte, and $Sm_{0.5}Sr_{0.5}CoO_{3-\delta}$ (SSCo)-SDC (weight ratio 75:25) as the cathode. The active area is 0.23 cm^2 for Cell #1 and 0.34 cm^2 for Cell #1, respectively. The details about material, structure, and processing methods for both Cell #1 and Cell #2 are listed in Table 1.

Table 1. Summary of materials, structures, and processing methods for Cell #1 and Cell #2

Components		Substrate	Anode	Electrolyte	Cathode
Cell #1	Material	SS430	NiO-SDC	ScSz/SDC	SSCo-SDC
	Processing		Screen printing	PLD [1]	Screen printing
	Thickness		90μm	2/20μm	25μm
Cell #2	Material	Hastelloy X	NiO-SDC	SDC	SSCo-SDC
	Processing		SPS [2]	SPS	Screen printing
	Thickness		30μm	30μm	45μm

[1] Pulsed laser deposition
[2] Suspension plasma spray

Both cells were mounted on an alumina tube using Ceramabond 552 (Aremco). Pt meshes were used as both anode and cathode current collectors. Both cells were heated to 650°C at 2°C/min and dwelled at 650°C for 5 hours for the purpose of fully reducing the anodes by gradually raising the hydrogen concentration (maintaining 3% water stream). Subsequently, these 2 cells were heated to 800°C at 3°C/min to sinter the cathode for 30 min, and then cooled

down to desired temperatures at 2°C/min successively for EIS and current-voltage-power curve measurement.

Voltage-Current (I-V) curves were measured using Solartron 1480A potentiostat with a scan rate of 4 mV/sec in the potential range from open circuit voltage (OCV) to 0.3 V. EIS was measured over the frequency range of 100 kHz to 0.1Hz with a Solartron 1260 frequency response analyzer (FRA) connected to a Solartron 1480A potentiostat. The perturbation amplitude was set to 50 mV at open circuit. For each temperature of 600°C, 550°C, 500°C, 450°C and 400°C, both impedance and I-V data were measured twice at 10-minute interval at designed temperature point. All above measurements were under conditions of moist hydrogen as the fuel and dry air as the oxidant.

The tested cells were immersed into epoxy followed by solidification, and then sectioned and polished with different diamond slurries. The 2 cells microstructures of cross-sections were then measured with a scanning electron microscope (SEM, Hitachi S-3500N) at two different resolutions described below.

3. Experimental results and discussions

3.1 Cell microstructures

In order to investigate microstructures affected by PLD and SPS, the two cells were characterized using SEM at different resolutions.
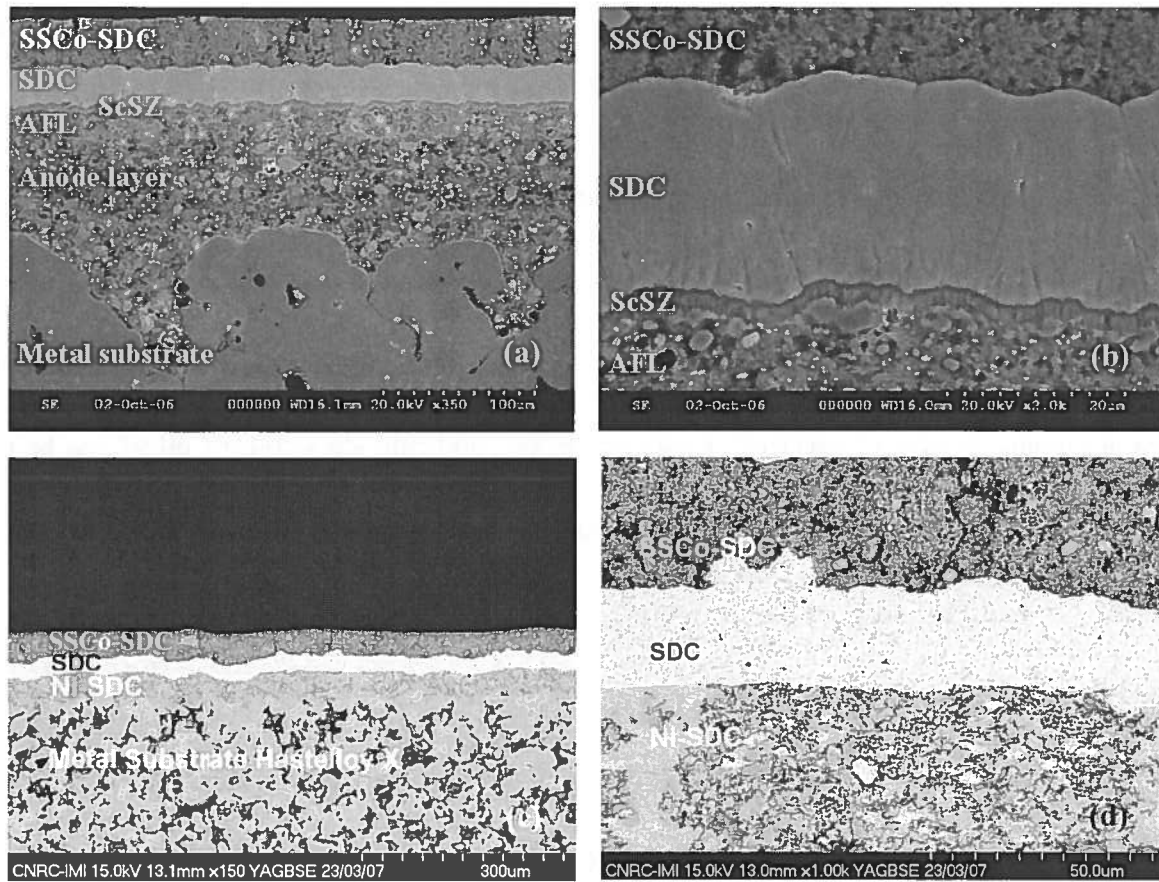
Fig. 1. Cross-sectional SEM images of the two tested cells: (a) ×150 magnification for Cell #1, (b) ×1000 magnification for Cell #1, (c) ×200 magnification for Cell #2. (d) ×2000 magnification for Cell #2

Fig. 1 clearly gives multi-layer microstructures of the cross-sections for Cell #1 and Cell #2. For both cells, the electrode layers are all porous, which are necessary for reactant gas feeds and diffuses. However, the interfaces between layers from the two cells are drastically different due to the processing methods.

In Fig. 1a and Fig. 1b for Cell #1, the AFL is much finer, not only extending the length of triple phase boundary to speed up the absorption/adsorption reaction of oxygen-ion, but also enhancing the bond of electrolyte/anode interface to reduce the interfacial contact resistance.

7

Our previous work indicated that various microstructures, density and interfacial properties of bi-layer ScSZ/SDC film could be achieved by controlling the process parameters of PLD technique [7]. The bi-layer electrolyte ScSZ/SDC fabricated by PLD at a very low temperature was fine and dense without any pinholes or cracks, which not only improves OCV [9] but also meets the requirement of gas-tightness. From the SEM images in Fig.1, it can be seen that no visible separation gaps between interfaces of both anode side and cathode side for Cell #1 can be found, suggesting the interface contacts were excellent.

Fig. 1c and Fig. 1d give microstructure of the cross-section for Cell #2 fabricated by SPS method, which has been well proven to be cost-effective and suitable for scale-up and offers an alternative technique to deposit SOFC functional layers on metal substrate [9]. Several tiny cracks were found in electrolyte layers for Cell #2, but none of them penetrated completely through the overall layer. Although in Fig. 1d no clear interfacial gap can be found on both sides of anode and cathode for Cell #2, suggesting relative strong interfacial contact, compared with Cell #1, the interfacial bonding of Cell #2 seems not to be as compact as the one of Cell #1. These interfacial differences could result in large differences in ohmic and polarization resistances of these two cells. This will be further discussed in the section 3.3.

3.2 Electrochemical Polarization

Fig. 2 shows the voltage-current and power-current curves for both Cell #1 and Cell #2 in a temperature range of 400~600°C. A thin ScSZ layer was employed for Cell #1 to block the elelctronic leaking from SDC electrolyte[8]. Cell #1 achieved an open circuit voltage (OCV) of

8

1.00~1.03 V, which is much higher than the OCV of 0.86~0.94 V for Cell #2 where only one single SDC layer of electrolyte was used. With respect to cell performance at the operation temperatures of 400°C, 450°C, 500°C, 550°C and 600°C, the maximum power densities of Cell #1 are 0.063W/cm^2, 0.097W/cm^2, 0.125W/cm^2, 0.144W/cm^2, and 0.161W/cm^2, respectively. The maximum power densities of Cell #2 are 0.015W/cm^2, 0.033W/cm^2, 0.073 W/cm^2, 0.123 W/cm^2, and 0.181 W/cm^2, respectively.
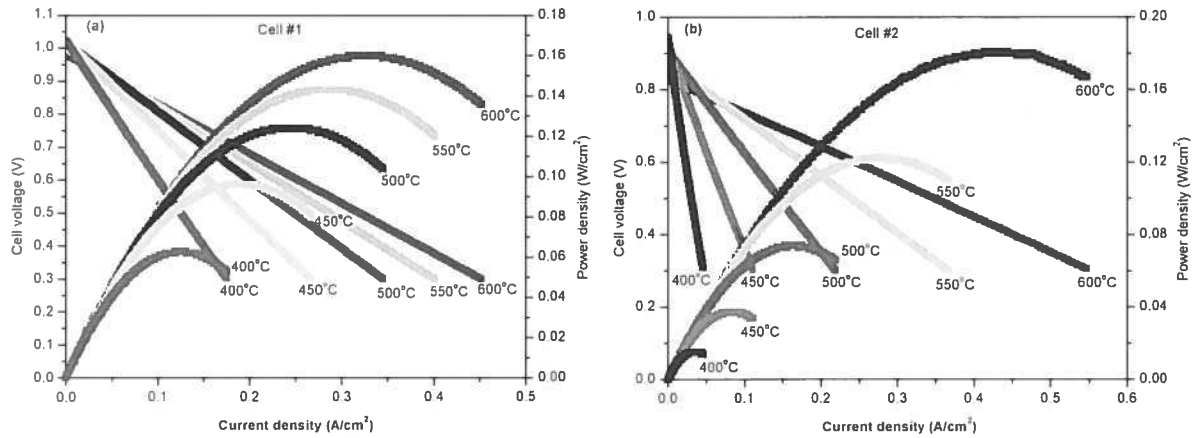

Fig. 2. Electrochemical polarization at temperatures of 400 ~ 600°C for Cell #1(a) and Cell #2 (b)

Fig. 3a and Fig. 3b show the open circuit voltage (OCV) and maximum power density (MPD) as a fuction of the operational temperatures for the two cells, respectively. As expected, the OCVs of the two cells decrease slightly while the MPD of both cells increase dramatically with the increase of operation temperature. One point should be noted that MPD of Cell #2 exceeds the one of Cell #1 over 600°C although the OCV of Cell #2 is still lower than the one of Cell #1. In order to understand these phenomena, the electrochemical impedances for both Cell #1 and Cell #2 were measured under open circuit condition.
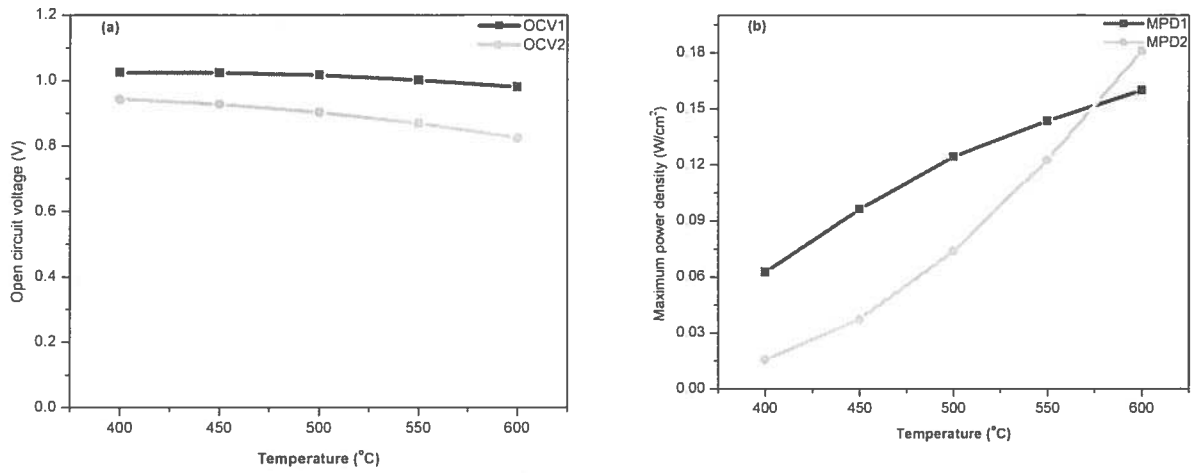
Fig. 3. (a) Open circuit voltage and (b) maximum power density of the metal-supported SOFCs over temperature range of 400- 600°C

3.3 Electrochemical Impedance Measurement

EIS has been recognized as a powerful diagnostic tool to investigate fundamental processes and various polarization losses for SOFCs [20]. In order to understand and compare various polarization losses and associated reaction kinetics for both Cell #1 and Cell #2, electrochemical impedances were measured under open circuit condition at temperatures of 400~600°C. Nyquist plots for Cell #1 and Cell #2 over temperature ranges of 400~600°C are shown in Fig. 4a and Fig. 4b, respectively.

10

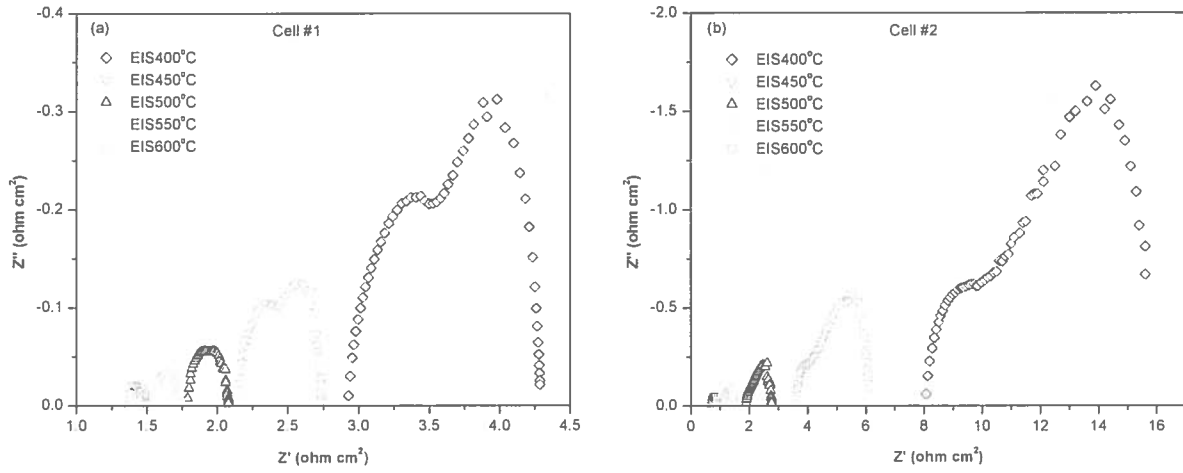Fig. 4. AC impedance spectra of two metal-supported cells under open circuit condition over temperature range of 400~600°C for Cell #1 (a) and Cell #2 (b)

Ohmic resistances R_e and polarization resistances R_p of the two cells at temperatures of 400~600°C were extracted from the measured Nyquist plots in Fig. 4, assuming cell resistance $R_t = R_p + R_e$. Generally speaking, the main contributor to R_e is from the electrolyte [21]. Fig. 5a, Fig.5b and Fig. 5c show curves of R_e, R_p, and R_t as a function of the operation temperature for the two cells, respectively. It can be seen that both of the ohmic resistances R_e and polarization resistances R_p of the two cells decrease with the increase of measurement temperature. R_e and R_p of cell #2 are obviously greater than the one of Cell #1 over the low temperature range of 400~500°C due to Cell #2 weaker bonding of the electrolyte-electrode interfaces than Cell #1 as shown in the Fig. 1. However R_e, R_p, and R_t of Cell #2 are more sensitive to the change of temperature than the ones of Cell #1 due to the energy difference of processing between PLD and SPS. Over 550°C, the large difference in polarization resistance for the two cells gradually disappears and almost convergent to a small value. The impact of fabrication processes becomes

11

less important when the reaction kinetics got enhanced at elevated temperature. In this situation, ohmic loss dominates the overpotential losses. Over 600°C, the ohmic resistance of Cell #2 becomes lower than the one of Cell #1 and this is most likely due to the low ionic conductivity of ScSZ in the bi-layer electrolytes and the potential reaction between ScSz and SDC in Cell #1. Hence ohmic resistance of Cell #2 becomes lower than the ohmic resistance of Cell #1. The lower cell resistance of Cell #2 is in agreement with the phenomenon in section 3.2: MPD of Cell #2 exceeds the one of Cell #1 over 600°C although the OCV of Cell #2 is still lower than the one of Cell #1.
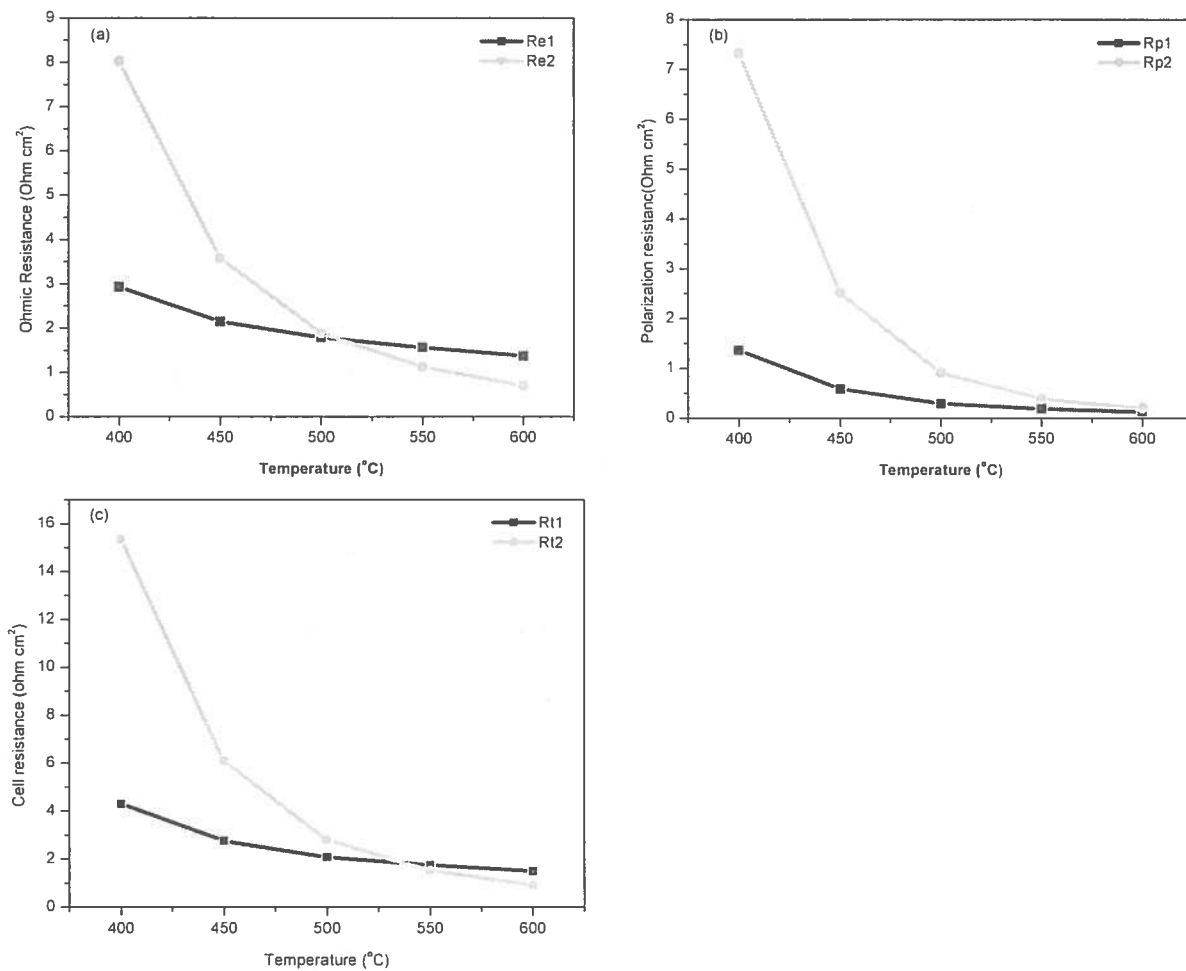
Fig. 5. (a) Ohmic resistances, (b) polarization resistances and (c) cell resistances of the two metal-supported cells over temperature range of 400~600°C under open circuit condition

3.4 Modeling of Cell Polarization

3.4.1 Analysis of Polarization Characteristics

In the simplest case, the electrochemical processes characterized for Cell #1 and Cell #2 in Fig.4 can be simulated by an equivalent circuit model (ECM) in Fig. 6a [22], where (R_1C_1) simulating high frequency processes, (R_2C_2) medium frequency processes, R_{ohm} ohmic resistance mainly consisting of electrolyte resistance and various contact resistances, L an inductance introduced by connecting conductor. The time constants of the electrochemical processes are given by RC and can be determined through frequency response measurements [23]. It is also well known that I-V characteristics reflect the overall effect of ohmic polarization, concentration polarization, and activation polarization. Hence, DC measurement and analysis of steady-state I-V characteristics are an effective way to investigate reaction kinetics for SOFCs [21], although the capacitive and inductance parts in Fig. 6a could not be reflected in I-V characteristics. The ECM in Fig. 6b is applied to analyze I-V polarization characteristics for Cell #1 and Cell #2 [24], where E_{ocv} open circuit voltage, η_{act} activation polarization, η_{con} concentration polarization, η_{ohm} ohmic polarization, R_{load} load resistance, V cell voltage, i current density.
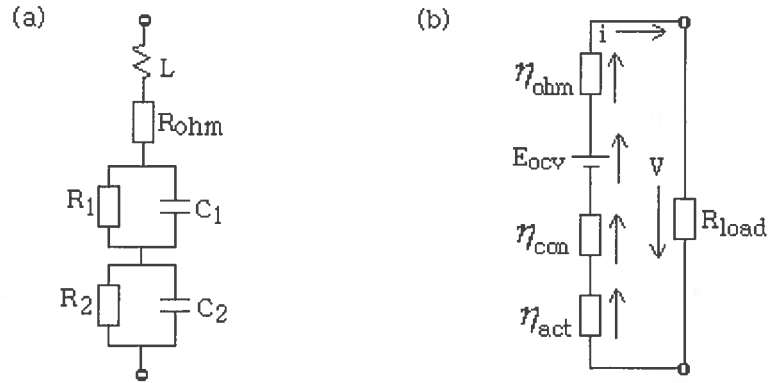
Fig. 6. Two equivalent circuit models (ECM) for metal-supported SOFC: (a) ECM to simulate the electrochemical processes under open circuit condition; (b) ECM to analyze I-V polarization characteristics

Previous experimental results [25] [26] suggested the overpotential on the anode side was extremely small in comparison to the one on the cathode side. Thus, activation polarization and concentration polarization from the anode side could be ignored for simplification of the analysis. As a result, cell voltage $V(i) = E_{ocv} - \eta_{act} - \eta_{ohm} - \eta_{conc}$ can be simplified

$$V(i) = E_{ocv} - \eta_{act,c} - \eta_{ohm} - \eta_{con,c} \tag{1}$$

In this work, flow rates of fuel and oxidant were held high enough compared to the stoichiometry required by the corresponding current density, thus concentration polarization could be simply treated either as a constant or be ignored. This allows further simplify the cell voltage:

$$V(i) = E_{ocv} - \eta_{act,c} - \eta'_{ohm} \tag{2}$$

where $\eta'_{ohm} = \eta_{ohm} + \eta_{con,c}$. The activation polarization for the cathode is normally expressed by the well-known Butler-Volmer equation [23]

14

$$i = i_{0,c}\left\{\exp\left(\frac{\beta n_e F \eta_{act,c}}{RT}\right) - \exp\left(-\frac{(1-\beta)n_e F \eta_{act,c}}{RT}\right)\right\} \tag{3}$$

where i is current density (mA/cm^2), $i_{0,c}$ cathode exchange current density (mA/cm^2), β the transfer coefficient (usually 0.5) [27], n_e electrons transferred per reaction (here 2), F Faraday constant (96485 C mol^{-1}), $\eta_{act,c}$ cathode activation polarization (V), R universal gas constant (8.314Jmol^{-1}k^{-1}), T temperature (K). If we defined $\eta_0(T)$ as:

$$\eta_0(T) = \frac{RT}{\beta n_e F} \tag{4}$$

Then, Eq. (3) can be expressed as

$$i = i_{0,c}\left\{\exp\left(\frac{\eta_{act,c}}{\eta_0(T)}\right) - \exp\left(-\frac{\eta_{act,c}}{\eta_0(T)}\right)\right\} \tag{5}$$

For high activation polarization, it is possible that

$$\eta_{act,c} \gg \eta_0(T) \tag{6}$$

In such case, Eq. (3) can be simplified as the logarithmic current-potential relation

$$\eta_{act,c} = -\frac{RT}{\beta n_e F}\ln i_{o,c} + \frac{RT}{\beta n_e F}\ln i \tag{7}$$

Eq. (7) is the well–known Tafel equation for the cathode. One point has to be noted that Eq. (7) is only valid for $i > i_{0,c}$ [28].

For low activation polarization, it is possible that

$$\eta_{act,c} \ll \eta_0(T) \tag{8}$$

In such case, Butler-Volmer equation can be simplified as the linear current-potential relation in terms of Taylor series expansion

$$\eta_{act,c} = i\frac{RT}{n_e F i_{0,c}} \qquad (9)$$

By differentiating Eq. (9), we can define

$$R_{ct,c}^{ocv} \overset{def}{=} \frac{\partial \eta_{act,c}}{\partial i} = \frac{RT}{n_e F i_{0,c}} \qquad (10)$$

where $R_{ct,c}^{ocv}$ is cathode charge transfer resistance under open circuit condition [29][30]. When both concentration polarization of the whole cell and activation polarization on the anode side are neglected as discussed above, polarization resistances R_p obtained from EIS measurement under open circuit conditions for Cell #1 and Cell #2 can be approximately regarded as $R_{ct,c}^{ocv}$, i.e.

$$R_{ct,c}^{ocv} \approx R_p \qquad (11)$$

Based on Eq. (10) and the approximation of $R_{ct,c}^{ocv}$ via Eq. (11), the cathode exchange current density $i_{0,c}$ could be calculated. The calculated exchange current density $i_{0,c}$ and the current density i^* corresponding to MPD for Cell #1 and Cell #2 at operation temperatures of 400~600°C are listed in Table 2. It is obvious that cathode exchange current density $i_{0,c}$ increases dramatically with the increase in operating temperatures for both cells, so does the current density i^*, and the $i_{0,c}$ for Cell #1 is greater than the $i_{0,c}$ for Cell #2 at given temperatures. Subsequently, the increase of the cathode exchange current density $i_{0,c}$ as a function of temperature extend the range of current density that is not valid for the Tafel equation, but is still valid for linear activation polarization via Eq. (9) as discussed above. Moreover, the calculated cathode exchange current density, as functions of both operation

temperatures, offers a viewpoint to reveal the polarization related to fabrication processes and

materials properties for SOFCs.

Table 2. Calculated exchange current density for cathode and measured current density corresponding to MPD at operation temperatures from 400~600°C

Temperature (°C)		400	450	500	550	600
Cell #1	$i_{0,c}$ (mA/cm2)[1]	21.3	53.0	114.1	190.2	298.1
	i^* (mA/cm2)[2]	108.0	173.0	225.0	263.0	308.0
Cell #2	$i_{0,c}$ (mA/cm2)	4.0	12.4	37.0	92.5	184.7
	i^* (mA/cm2)	26.0	71.0	153.0	257.0	414.0

[1] cathode exchange current density (mA/cm^2)
[2] current density corresponding to MPD (mA/cm^2)

With Eq. (2) we can get $\eta_{act,c}(i) = E_{ocv} - V(i) - \eta'_{ohm}(i)$, where i is current density at

different temperatures of 400~600°C as listed in Table 2, $\eta'_{ohm}(i) \approx i\, R_{ohm}$, R_{ohm} ohmic resistance

obtained from EIS measurement. Consequently, we could approximately calculate $\eta_{act,c}(i)$ at

different temperatures of 400~600°C in order to investigate the cathode activation polarization

over the current density range of $0 \sim i^*$. The values of $\eta_0(T)$, $\eta_{1act,c}$, and $\eta_{2act,c}$ at current

density of i^* at temperatures of 400~600°C were listed in Table 3. The calculated results listed

in Table 3 indicated that Eq. (8) was not strictly applicable at current density of i^*. Chan et al

discussed the two special situations including high activation polarization and low activation

polarization [27]. In terms of the applicable range of these two simplified activation models via

Eq. (7) and Eq. (9) discussed by Chan et al, the low activation polarization situation is more

suitable to the calculated cathode activation polarization $\eta^*_{act,c}$ at current density i^*. On one

hand, activation polarization corresponding to the current density i^* is maximized in the range of

$0 \sim i^*$. On the other hand, considering the activation polarizations on the anode side and

concentration polarization of the cell are ignored, the calculated cathode activation polarization

$\eta_{act,c}$ is expected to be greater than the virtual activation polarization. As a result, with respect

to the investigated current density range of $0 \sim i^*$, it is reasonable to employ linear model via Eq.

(9) to approximate the activation polarization of Cell #1 and Cell #2. The reduction of the

activation polarization with increase of temperature strengthens the linearity of activation

polarization as indicated by Eq. (8). Table 3 suggests that Cell #1 exhibited less activation

polarization than Cell #2 at each given temperature.

Table 3. Calculated values of $\eta_0(T)$, η^*_{1act} and η^*_{2act} at operation temperatures of 400~ 600°C

Temperature (°C)	400	450	500	550	600
$\eta_0(T)$ (mV)[1]	58.0	62.3	66.6	70.9	75.2
$\eta^*_{1act,c}$ (mV)[2]	136.5	99.2	66.7	48.3	40.5
$\eta^*_{2act,c}$ (mV)[3]	173.3	160.1	133.6	108.1	102.1

[1] $\eta_0(T) = \dfrac{RT}{\beta n_e F}$

[2] cathode activation polarization at current density i^* for Cell #1

[3] cathode activation polarization at current density i^* for Cell #2

3.4.2 Fitting the experimental data with the model

According to the discussion for the activation polarization above, Eq. (2) can be completely linearized over the investigated current range of $0 \sim i^* $ mA

$$V(i) = E_{ocv} - iR_{act,c} - iR_{ohm} = E_{ocv} - iR_t \tag{12}$$

where $R_t = R_{act,c} + R_{ohm}$ $\tag{13}$

With the measured current-voltage data and approximated Eq. (12), the values of fitted parameters such as open circuit voltage E'_{ocv} and cell resistance R'_t could be obtained through the fitting function Polyfit in Matlab, as listed in Table 4 and Table 5, respectively. Subsequently, the normalized and accumulated-residuals (NA-Res) of I-V curve fitting with Eq. (12) at operation temperatures of $400^{\circ}C \sim 600^{\circ}C$ is calculated via

$$NA - Res = \frac{100}{N} \sum_i \left| V_{measured} - V_{calculated} \right|_T \tag{14}$$

where $V_{measured}$ is the measured value of cell voltage; $V_{calculated}$, calculated value of cell voltage via Eq. (12) with parameters from I-V curve fitting; N, the number of data points for current density range of $0 \sim i^*$; T, temperature.

Table 4. Fitted E'_{ocv} and measured E_{ocv} at operation temperatures of $400 \sim 600^{\circ}C$

Temperature ($^{\circ}$C)		400	450	500	550	600
Cell #1	$E_{ocv}{}^1$ (V)	1.0244	1.0238	1.0167	1.0014	0.9801
	$E'_{ocv}{}^2$ (V)	1.0241	1.0247	1.0180	1.0023	0.9813
Cell #2	E_{ocv} (V)	0.9440	0.9291	0.9040	0.8701	0.8258
	E'_{ocv} (V)	0.9404	0.9257	0.9054	0.8740	0.8316

Table 5. Fitted R_t' and measured R_t at operation temperatures of 400~600°C

Temperature (°C)		400	450	500	550	600
Cell #1	R_t [1] (Ohm cm2)	4.2854	2.7360	2.0784	1.7459	1.4951
	R_t' [2] (Ohm cm2)	4.2273	2.7348	2.0856	1.7498	1.5025
Cell #2	R_t (Ohm cm2)	15.3496	6.0884	2.7851	1.5042	0.8961
	R_t' (Ohm cm2)	14.8022	5.8597	2.7918	1.5564	0.9511

[1] cell resistance from EIS measurement under open circuit condition

[2] cell resistance from I-V fitting via Eq. (12)

Table 6. Normalized and accumulated-residuals (NA-Res) of I-V fitting at operation temperatures of 400~600°C

Temperature (°C)		400	450	500	550	600
NA-Res[1]	Cell #1	0.1334	0.0735	0.0555	0.0462	0.0398
(V)	Cell #2	0.4052	0.2195	0.0932	0.0855	0.1406

$$[1]\ NA-Res = \frac{100}{N}\sum_i |V_{measured} - V_{calculated}|_T$$

Table 4 and Table 5 indicated that the fitted cell resistance and open circuit voltage agreed well with the measured cell resistance and open circuit voltage. Table 6 shows that normalized

20

and accumulated-residuals of linear fitting were quite small with ranges from 0.0398 V to 0.4052 V related to each 100 current points at the temperatures of 400~600°C. These results suggest that the approximation and discussion on the activation polarization and I-V characteristics above was reasonable and feasible. Moreover, normalized and accumulated-residuals NA-Res of Cell #1 was much lower than that of Cell #2 at each given temperature.

With the fitted open circuit voltage E'_{ocv} and cell resistance R'_t through fitting at temperatures of 400~600°C, the cell MPD can be predicted in terms of $P_{max} = \dfrac{1}{2}\dfrac{{E'_{ocv}}^2}{R'_t}$ conveniently. As indicated from the results in Table 7, the lower the operation temperature, the higher the prediction precision for MPD. In addition, Cell #1 exhibits higher prediction precision than Cell #2 at given operation temperatures. These results are consistent with the linearity of activation polarization at temperatures of 400~600°C.

Table 7. Measured *MPD* and Simulated *MPD'* at different operational temperatures of 400°C~ 600°C

Temperature (°C)		400	450	500	550	600
Cell #1	MPD^1 (W/cm2)	0.0626	0.0963	0.1244	0.1435	0.1600
	MPD'^2 (W/cm2)	0.0606	0.0937	0.1220	0.1432	0.1633
Cell #2	MPD (W/cm2)	0.0155	0.0374	0.0738	0.1227	0.1810
	MPD' (W/cm2)	0.0159	0.0395	0.0811	0.1404	0.2186

[1] measured MPD
[2] simulated MPD

4. Conclusions

Polarization characteristics related to fabrication processes and operating temperatures have been investigated for metal-supported SOFCs fabricated by PLD and SPS, respectively. With EIS and current-voltage polarization curves, the electrochemical mechanism for the linear polarization characteristics of the metal-supported SOFCs has been addressed according to cathode exchange current density, polarization loss and maximum power density over temperature range of 400~600°C. Experimental and simulating results indicated that high operating temperatures could extend the range of current density with linear activation polarization characteristics, and low activation polarization due to fabrication processes could also strengthen the linear range of activation polarization. In summary, fabrication processes and operation temperatures play an important role in the polarization characteristics of metal-supported SOFCs. The presented method in this manuscript also offers a viewpoint to reveal the polarization characteristics of SOFCs related to materials properties, fabrication processes, and operation temperatures.

Acknowledgements

References

[1] J. P. P. Huijsmans, F. P. F. van Berkel, G. M. Christie, J. Power Sources 71 (1998) 107-110.

[2] F. Nishiwaki, T. Inagaki, J. Kano, J. Akikusa, N. Murakami, K. Hosoi, J. Power Sources 157 (2006) 809-815.

[3] M. C. Tucker, G. Y. Lau, C. P. Jacobson, L. C. DeJonghe, S. J. Visco, J. Power Sources 171 (2007) 477-482.

[4] P. S. Patil, Materials Chemistry and Physics 59 (1999) 185-198.

[5] D. Perednis, L. J. Gauckler, Solid State Ionics 166 (2004) 229-239.

[6] J. Will, A. Mitterdorfer, C. Kleinlogel, D. Perednis, L. J. Gauckler, Solid State Ionics 131 (2000) 79-96.

[7] D. Yang, X. Zhang, S. Nikumb, C. Decès-Petit, R. Hui, R. Maric, D. Ghosh, J. Power Sources 164 (2007) 182-188.

[8] R. Hui, D. Yang, Z. Wang, S. Yick, C. Decès-Petit, W. Qu, A. Tuck, R. Maric, D. Ghosh, J. Power Sources 167 (2007) 336-339.

[9] R. Hui, Z. Wang, O. Kesler, L. Rose, J. Jankovic, S. Yick, R. Maric, D. Ghosh, J. Power Sources 170 (2007) 308-323.

[10] Z. Wang, J. Oberste-Berghaus, S. Yick, C. Decès-Petit, W. Qu, R. Hui, R. Maric, D. Ghosh, J. Power Sources, *accepted*.

[11] T. Suzuki, I. Kosacki, H.U. Anderson, Solid State Ionics 151 (2002) 111-121.

[12] H.U. Anderson, M.M. Nasrallah, C.C. Chen, U.S. Patent, 5494700, 1996.

[13] R. Hui, Z.W. Wang, S. Yick, R. Maric, D. Ghosh, J. Power Sources 172 (2007) 840-844.

[14] G.M. Christie, F.P.F. van Berkel, Solid State Ionics 83 (1996) 17-27.

[15] W. Bai, K. L. Choy, R. A. Rudkin, B. C. H. Steele, Solid State Ionics, 113-115 (1998) 259-263.

[16] T. Suzuki, I. Kosacki, H.U. Anderson, P. Colomban, J. Am. Ceram. Soc. 84 (2001) 2007-2014.

[17] J.L.M. Rupp, L.J. Gauckler, Solid State Ionics 177 (2006) 2513-2518.

[18] A. Tschöpe, R. Birringer, Journal of Electroceramics 7 (2001) 167-177.

[19] R. Hui, J. Roller, S. Yick, X.G. Zhang, C. D. Petit, Y.S. Xie, R. Maric, D. Ghosh, Journal of Power Sources 172 (2007) 493-502.

[20] Q.A. Huang, R. Hui, B. Wang, J. Zhang, Electrochimica Acta 52 (2007) 8144-8164.

[21] S.B. Adler, Chem. Rev. 104 (2004) 4791-4843.

[22] Z.W. Wang, M.J. Cheng, Y.L. Dong, M. Zhang, H.M. Zhang, J. Power Sources 156 (2006) 306-310.

[23] S.C. Singhal and K. Kendal, High Temperature Solid Oxide Fuel Cells Fundamentals, Design and Applications, Elsevier Ltd., Oxford, England (2003).

[24] T. A. Aloui, K. Halouani, Applied Thermal Engineering 27 (2007) 731-737.

[25] C.R. Xia and M.L. Liu, Adv. Mater. **14** (2002) 521-523.

[26] T. Kato, K. Nozaki, A. Negishi, K. Kato, A. Momma, Y. Kaga, S. Nagata, K. Takano, T. Inagaki, H. Yoshida et al., J. Power Sources **133** (2004) 169-174.

[27] S. H. Chan, K. A. Khor, Z. T. Xia, J. Power Sources 93 (2001) 130-140.

[28] J. Larminie and A. Dicks, Fuel Cell Systems Explained (second edition), John Wiley & Sons, Chichester, England (2003).

[29] J. L. Zhang, Y.H. Tang, C.J. Song, J.J. Zhang, H.J. Wang, J. Power Sources 163 (2006) 532-537.

[30] C.J. Song, Y.H. Tang, J. L. Zhang, J.J. Zhang, H.J. Wang, J. Shen, S. McDermid, J. Li, P. Kozak, Electrochimica Acta 52 (2007) 2552-2561.